



WITNESSING THE BIRTH OF THE RED SEQUENCE: ALMA HIGH-RESOLUTION IMAGING OF [C II] AND DUST IN TWO INTERACTING ULTRA-RED STARBURSTS AT $z = 4.425$

I. OTEO^{1,2}, R. J. IVISON^{1,2}, L. DUNNE^{1,3}, I. SMAIL^{4,5}, A. M. SWINBANK^{4,5}, Z.-Y. ZHANG^{1,2}, A. LEWIS¹, S. MADDOX^{1,3}, D. RIECHERS⁶, S. SERJEANT⁷, P. VAN DER WERF⁸, A. D. BIGGS², M. BREMER⁹, P. CIGAN³, D. L. CLEMENTS¹⁰, A. COORAY¹¹, H. DANNERBAUER¹², S. EALES³, E. IBAR¹³, H. MESSIAS¹⁴, M. J. MICHAŁOWSKI¹, I. PÉREZ-FOURNON^{15,16}, AND E. VAN KAMPEN²

¹ Institute for Astronomy, University of Edinburgh, Royal Observatory, Blackford Hill, Edinburgh EH9 3HJ UK; ivanoteogomez@gmail.com

² European Southern Observatory, Karl-Schwarzschild-Str. 2, D-85748 Garching, Germany

³ School of Physics and Astronomy, Cardiff University, The Parade, Cardiff CF24 3AA, UK

⁴ Centre for Extragalactic Astronomy, Department of Physics, Durham University, South Road, Durham DH1 3LE UK

⁵ Institute for Computational Cosmology, Department of Physics, Durham University, South Road, Durham DH1 3LE, UK

⁶ Department of Astronomy, Cornell University, Ithaca, NY 14853, USA

⁷ Department of Physical Sciences, The Open University, Milton Keynes, MK7 6AA, UK

⁸ Leiden Observatory, Leiden University, P.O. Box 9513, NL-2300 RA Leiden, The Netherlands

⁹ H.H. Wills Physics Laboratory, University of Bristol, Tyndall Avenue, Bristol BS8 1TL, UK

¹⁰ Physics Department, Blackett Lab, Imperial College, Prince Consort Road, London SW7 2AZ, UK

¹¹ Department of Physics and Astronomy, University of California, Irvine, CA 92697, USA

¹² Universität Wien, Institut für Astrophysik, Türkenschanzstrasse 17, 1180 Wien, Austria

¹³ Instituto de Física y Astronomía, Universidad de Valparaíso, Avda. Gran Bretaña 1111, Valparaíso, Chile

¹⁴ Instituto de Astrofísica e Ciências do Espaço, Universidade de Lisboa, OAL, Tapada da Ajuda, PT1349-018 Lisboa, Portugal

¹⁵ Instituto de Astrofísica de Canarias, E-38205 La Laguna, Tenerife, Spain

¹⁶ Universidad de La Laguna, Dpto. Astrofísica, E-38206 La Laguna, Tenerife, Spain

Received 2016 January 25; revised 2016 June 5; accepted 2016 June 13; published 2016 August 4

ABSTRACT

Exploiting the sensitivity and spatial resolution of the Atacama Large Millimeter/submillimeter Array, we have studied the morphology and the physical scale of the interstellar medium—both gas and dust—in SGP 38326, an unlensed pair of interacting starbursts at $z = 4.425$. SGP 38326 is the most luminous star bursting system known at $z > 4$, with a total IR luminosity of $L_{\text{IR}} \sim 2.5 \times 10^{13} L_{\odot}$ and a star formation rate of $\sim 4500 M_{\odot} \text{ yr}^{-1}$. SGP 38326 also contains a molecular gas reservoir among the most massive yet found in the early universe, and it is the likely progenitor of a massive, red-and-dead elliptical galaxy at $z \sim 3$. Probing scales of ~ 0.1 or ~ 800 pc we find that the smooth distribution of the continuum emission from cool dust grains contrasts with the more irregular morphology of the gas, as traced by the [C II] fine structure emission. The gas is also extended over larger physical scales than the dust. The velocity information provided by the resolved [C II] emission reveals that the dynamics of the two interacting components of SGP 38326 are each compatible with disk-like, ordered rotation, but also reveals an ISM which is turbulent and unstable. Our observations support a scenario where at least a subset of the most distant extreme starbursts are highly dissipative mergers of gas-rich galaxies.

Key words: galaxies: high-redshift – galaxies: ISM – galaxies: starburst – submillimeter: galaxies

1. INTRODUCTION

Surveys in the far-infrared (FIR) and (sub)-millimeter have revolutionized our understanding of the formation and evolution of galaxies, revealing a population of dusty starbursts at $z > 1$ that are forming stars at tremendous rates (Blain et al. 2002; Chapman et al. 2005; Weiß et al. 2009; Casey et al. 2013; Geach et al. 2013). At $z > 4$ these starbursts can be linked to the formation of the so-called red-sequence—passively evolving, early type galaxies which dominate the cores of clusters out to at least $z \sim 1.5$ (e.g., Stanford et al. 2006; Mei et al. 2009; Rosati et al. 2009; Strazzullo et al. 2010; Tozzi et al. 2015). While the bulk of star formation in the general population of galaxies occurred in the period since $z \sim 2$ (Sobral et al. 2013), red-sequence galaxies at $z > 1.5$ formed the bulk of their stellar population at much earlier times and over a brief time interval (Thomas et al. 2005, 2010). Therefore, analyzing strong starbursts at $z > 4$ is a way to study the likely progenitors of the most massive elliptical galaxies at $z > 1.5$ and consequently the birth of the galaxy red sequence, which might have appeared as early as $z > 2$ (Kodama et al. 2007; Zirm et al. 2008; Kriek et al. 2008; Gabor & Davé 2012; Hartley et al. 2013).

Herschel extragalactic imaging surveys such as *Herschel*-ATLAS (Eales et al. 2010) and HerMES (Oliver et al. 2010) have covered about 1000 deg^2 to the SPIRE confusion limit. As a consequence, the number of known dusty starbursts has increased from several hundred to several hundred thousand. Most of these are at $z < 3$, but there is also a population of sources at $z > 4$. Dusty starbursts at $z > 4$ can be found by looking for galaxies whose far-IR (FIR) spectral energy distributions (SEDs) rise from 250 to $500 \mu\text{m}$, so that their thermal dust emission peak is redshifted close to, or beyond $500 \mu\text{m}$. These are called $500 \mu\text{m}$ risers. Using H-ATLAS data, we have built a sample of dusty starbursts at $z > 4$ whose SPIRE flux densities satisfy $S_{500 \mu\text{m}}/S_{250 \mu\text{m}} > 2$ and $S_{500 \mu\text{m}}/S_{350 \mu\text{m}} > 1$, and we refer to these as ultrared starbursts (R. Ivison et al. 2016, in preparation). The resulting population was inspected by eye in each SPIRE band to exclude blended sources, checked for contamination by radio-loud active galactic nuclei (AGNs) and correlated with deep WHT/VISTA/Gemini optical/NIR imaging to reject any lenses that might have crept in despite our low median $S_{500 \mu\text{m}} \sim 50 \text{ mJy}$. Over 150 of these $500 \mu\text{m}$ risers were followed up with SCUBA-2 (Holland et al. 2013) and LABOCA (Siringo

et al. 2009) to improve FIR photometric redshifts and select only those whose colors are consistent with $z > 4$ by imposing $S_{870\ \mu\text{m}}/S_{500\ \mu\text{m}} > 0.4$.

In this paper we present Atacama Large Millimeter/submillimeter Array (ALMA) high-spatial resolution ($\sim 0''.1$) observations of dust and gas (traced by [C II] emission) in HATLAS J000307–330250, also known as SGP 38326, one of our ultra-red starbursts confirmed to be at $z = 4.425$ via multi-CO line detection. In Section 2 we give a description of the ALMA data used in this work and how they were reduced and analyzed. In Section 3 we present and discuss the main results of this work, regarding the properties of SGP 38326: detected emission lines, the implied molecular gas mass, morphology of dust and atomic gas, etc. Finally, Section 4 summarizes the main conclusions of this work. The total IR luminosities (L_{IR}) reported in this work refer to the integrated luminosities between rest-frame 8 and 1000 μm . Throughout this paper, the reported star formation rates (SFRs) are derived from the total IR luminosities ($L_{\text{IR},8-1000\ \mu\text{m}}$) assuming a Salpeter IMF and the Kennicutt (1998) calibration. Unless explicitly specified, the areas are calculated by carrying out 2D elliptical Gaussian fits and using $A = \pi \times R_1 \times R_2$, where R_1 and R_2 are the semi axes of the best-fitting elliptical gaussians, $R_1 = \text{FWHM}_1/2$ and $R_2 = \text{FWHM}_2/2$. All values taken from the literature are re-scaled to be consistent. We assume a flat universe with $(\Omega_m, \Omega_\Lambda, h_0) = (0.3, 0.7, 0.7)$, and all magnitudes are listed in the AB system (Oke & Gunn 1983). For this cosmology, the sky scale is $\sim 6.6\ \text{kpc}''$ at $z = 4.425$, the redshift of SGP 38326.

2. ALMA DATA

This work makes use of ALMA data from two different projects. Project 2013.1.00449.S was aimed at deriving redshifts via spectral scans in the ALMA 3 mm window (PI. A. Conley) of a sample of ultra-red starbursts at $z > 4$ of which SGP 38326 was a part. Project 2013.1.00001.S was a high-spatial resolution study of the dust continuum morphology at 870 μm of a subsample of our ultra-red starbursts (PI. R.J. Ivison) of which SGP 38326 was also a part. The ALMA data corresponding to the two projects were calibrated by using the ALMA pipeline and by executing different ALMA calibration scripts depending on the date when the data were released. The calibrated visibilities for the calibrators and science target were visually inspected and only very minor further flagging was required. The calibrated visibilities of the science target were then imaged in CASA by using a NATURAL weighting scheme to maximize sensitivity. The different tunings of the ALMA 3 mm spectral scan were carried out at different dates with the array in different configurations. Therefore, the beam size is different for each tuning. In this work we only use the ALMA 3 mm data corresponding to the tunings where the $^{12}\text{CO}(4-3)$ and $^{12}\text{CO}(5-4)$ lines were detected. The beam sizes were $1''.5 \times 1''.2$ and $1''.1 \times 1''.0$ for the $^{12}\text{CO}(4-3)$ and $^{12}\text{CO}(5-4)$ transitions, respectively. The rms of the $^{12}\text{CO}(4-3)$ and $^{12}\text{CO}(5-4)$ observations are $0.54\ \text{mJy beam}^{-1}$ and $0.64\ \text{mJy beam}^{-1}$, respectively, in $50\ \text{km s}^{-1}$ channels. The beam size of the 870 μm observations is $0''.16 \times 0''.12$, which corresponds to a physical scale of about $1.0\ \text{kpc} \times 790\ \text{pc}$. The rms of the 870 μm continuum map is $0.11\ \text{mJy beam}^{-1}$.

The redshift of SGP 38326 was unknown when the 870 μm continuum ALMA observations were performed. Fortunately, its redshifted [C II] emission was covered by the default

continuum setup, offering a unique opportunity to study the ISM of intense starbursts at $z > 4$ at unprecedented spatial resolution. The rms in the spectral window where [C II] is detected is $0.66\ \text{mJy beam}^{-1}$ in $100\ \text{km s}^{-1}$ channels, and the beam size is $0''.16 \times 0''.12$ or about $1.0\ \text{kpc} \times 790\ \text{pc}$ for the assumed cosmology.

3. SGP 38326: A PAIR OF INTERACTING STARBURSTS AT $z = 4.425$

SGP 38326 (R.A. = 00:03:07.2, decl. = $-33:02:50.9$) was selected in the South Galactic Pole field of the Herschel-ATLAS (Eales et al. 2010, E. Valiante et al. 2016, in preparation) as a 500 μm riser (see Section 1). The SPIRE flux densities of SGP 38326 are $S_{250\ \mu\text{m}} = 29 \pm 5\ \text{mJy}$, $S_{350\ \mu\text{m}} = 29 \pm 6\ \text{mJy}$, $S_{500\ \mu\text{m}} = 46 \pm 7\ \text{mJy}$. SGP 38326 was subsequently observed with SCUBA-2 at 870 μm ($S_{870\ \mu\text{m}} = 33 \pm 4\ \text{mJy}$), and by fitting a set of FIR templates to its SPIRE and SCUBA-2 flux densities, we determined a best-fit photometric redshift $z_{\text{phot}} \sim 4.5$.

The ALMA spectral scan from program 2013.1.00449.S in the 3 mm window confirmed its redshift to be $z = 4.425 \pm 0.001$ via detection of the $^{12}\text{CO}(4-3)$ and $^{12}\text{CO}(5-4)$ emission lines (Figure 1). The total IR luminosity of SGP 38326, obtained from an SED fit to the *Herschel* and SCUBA-2 flux densities, is $L_{\text{IR}} = (2.5 \pm 0.3) \times 10^{13} L_\odot$, implying a staggering IR-derived SFR $\sim 4500 M_\odot\ \text{yr}^{-1}$, among the strongest starbursts so far found in the early universe (see Table 1). The detected CO emission lines were extremely wide, $\text{FWHM}^{12}\text{CO}(4-3) = 1080 \pm 90\ \text{km s}^{-1}$ and $\text{FWHM}^{12}\text{CO}(5-4) = 1280 \pm 80\ \text{km s}^{-1}$, from Gaussian fits. This is compatible with SGP 38326 being a system of at least two starbursts in the process of interaction, as already seen in extreme starbursts at lower redshifts with similarly wide CO lines (Fu et al. 2013; Ivison et al. 2013). In fact, the $^{12}\text{CO}(5-4)$ observations resolved SGP 38326 into two interacting components, SMG1 and SMG2 (see Figure 2). The $^{12}\text{CO}(5-4)$ emission in SMG1 presents an elongated extension toward the southwest. This can be interpreted as a faint and relatively dust poor CO emitter interacting with SMG1 and SMG2, a CO bridge connecting the two interacting components (see also later in the text), or an outflow. The depth and resolution of the data are insufficient to fully discriminate between the possible scenarios. As discussed later, the [C II] velocity map shows no evidence of outflowing atomic gas and OH 163 μm emission (a tracer of molecular outflows) is not clearly detected in SMG1 despite the detection of the continuum at the line frequency (see Figure 1). The existence of a CO bridge is supported by the detection of similar structures in other systems of interacting starbursts at lower redshifts (Zhu et al. 2007; Fu et al. 2013; Appleton et al. 2015) and QSOs (Carilli et al. 2013). The velocity map of SMG1 obtained from the $^{12}\text{CO}(5-4)$ emission is compatible with an ordered rotation (see Figure 2). As shown in Section 3.6, this velocity structure is in agreement with that obtained from the [C II] emission at $\sim 10\times$ times better spatial resolution (see Section 3.6).

SGP 38326 is resolved into three 870 μm components (see Figure 2), as are many bright SMGs (Hodge et al. 2013; Karim et al. 2013; Bussmann et al. 2015; Simpson et al. 2015a, 2015b). SMG1 and SMG2 (Figure 3), the brightest components (see flux densities in Table 2), are both at the same redshift, $z = 4.425$. There is no [C II] or CO emission detected in SMG3 ($S_{870\ \mu\text{m}}^{\text{SMG3}} = 1.7 \pm 0.4\ \text{mJy}$), located $2''.2$

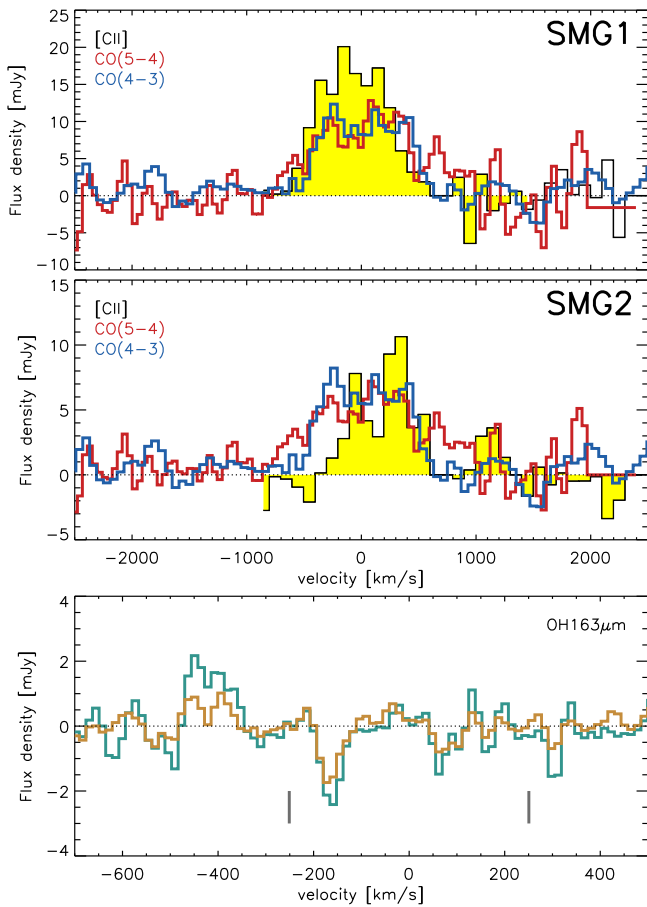


Figure 1. Upper and middle: unambiguous confirmation that SGP 38326 lies at $z = 4.425$ via detection of $^{12}\text{CO}(5-4)$ and $^{12}\text{CO}(4-3)$ in an ALMA 3 mm spectral scan. The CO lines shown correspond to the emission of SMG1 and SMG2. The [C II] emission of the two interacting components of SGP 38326 (see the text for more details) are also shown. The CO spectra have been re-scaled (multiply by 3 for $^{12}\text{CO}(5-4)$ and 6 for $^{12}\text{CO}(4-3)$) to match the flux scale of the [C II] line. Bottom: faint (or absent) OH $163\ \mu\text{m}$ emission in SMG1. The green curve represents the spectrum in the center of SMG1 (extracted from an aperture equal to one synthesized beam), where dust emission is at its maximum. The brown spectrum has been extracted using an aperture enclosing the whole area where [C II] emission is detected. Small vertical gray lines represent where the two components of the OH $163\ \mu\text{m}$ would be located assuming the redshift derived from the detected CO and [C II] lines. There is a narrow ($81 \pm 16\ \text{km s}^{-1}$, FWHM) emission line at $\sim -400\ \text{km s}^{-1}$ at the center of SMG1 (where the dust continuum emission is at its maximum) that we tentatively associate to OH $163\ \mu\text{m}$ emission (see details in Section 3.5). No OH $163\ \mu\text{m}$ emission or absorption is detected in SMG2 either (spectrum not shown for the sake of representation clarity). In all panels, the spectra shown were extracted after continuum subtraction.

away from SMG1. This might indicate that SMG3 has a different redshift than SMG1 and SMG2. However, SMG3 is about 14 times fainter than SMG1 and SMG2 combined. If we assume that the CO luminosity scales with the total IR luminosity, the peak flux of the CO lines would be much lower than the rms of the observations. The same is true for [C II], assuming again that its luminosity scales with the total IR luminosity. Therefore, with the current data, is not possible to clarify whether SMG3 is also interacting with SMG1 and SMG2. From now on, we focus our study on SMG1 and SMG2, the two clear components of the merging system. These are separated by $\sim 10\ \text{kpc}$ in the plane of the sky and their properties are summarized in Table 2.

Due to the high inferred luminosity of SGP 38326, we should consider whether its emission has been amplified by gravitational lensing. SGP 38326 has no near-IR counterpart in the VIKING survey (Edge et al. 2013); the closest VIKING-detected source is $\sim 7''5$ away. The 5σ limiting magnitudes of the VIKING survey range from 23.1 mag in the Z band to 21.2 mag in the K_s band. Assuming that any lens galaxy would be an elliptical, the limiting magnitude in Z would imply $I < 23.1$ mag. Therefore, the lack of VIKING detection would imply that any potential lensing galaxy would be significantly fainter than the lenses in the H-ATLAS survey discovered so far (Bussmann et al. 2013). Additionally, the dust continuum emission does not show any evidence of lensing, as it does in some ultra-red starburst at $z > 4$ (Oteo et al. 2016). Therefore, we suggest that neither of the two merging components is lensed, in contrast with other high- z extremely bright galaxies reported in the literature, such as HFLS3 (Riechers et al. 2013; Cooray et al. 2014), HDF 850.1 (Walter et al. 2012), HXMM01 (Fu et al. 2013) or HATLAS J084933 (Ivison et al. 2013).

3.1. A Massive Molecular Gas Reservoir

The integrated $^{12}\text{CO}(5-4)$ emission shown in Figure 2 can be used to estimate the total mass of the molecular gas reservoir in SGP 38326, as well as the molecular gas mass of each interacting component. We note that we have used the $^{12}\text{CO}(5-4)$ transition to derive the molecular gas mass of SMG1 and SMG2 because these observations provide better spatial resolution than the observations of the $^{12}\text{CO}(4-3)$ line. We assume that the average CO line ratio for SMGs (Carilli & Walter 2013), $L'_{\text{CO}(5-4)}/L'_{\text{CO}(1-0)} = 0.39$, is valid for SGP 38326. The molecular gas masses are then calculated using $\alpha_{\text{CO}} = 0.8 M_{\odot} (\text{K km s}^{-1} \text{pc}^2)$, a value typically assumed for high- z starbursts and local ULIRGs (Downes & Solomon 1998). The derived values are shown in Table 2. The total molecular gas of SGP 38326 ($M_{\text{g, total}} = M_{\text{g}}^{\text{SMG1}} + M_{\text{g}}^{\text{SMG2}}$ — see also Table 1) is higher than that in any other system so far studied at similar redshifts (see Table 1). We note that the calculation of the molecular gas mass from a single mid- J transition might be highly uncertain due to the effect that variation in excitation has on the CO line ratios. The total molecular gas mass of SGP 38326 derived from the $^{12}\text{CO}(4-3)$ is $\sim 2.8 \times 10^{11} M_{\odot}$ assuming the average $L'_{\text{CO}(4-3)}/L'_{\text{CO}(1-0)} = 0.46$ ratio for SMGs from Carilli & Walter (2013). The molecular gas determined from the $^{12}\text{CO}(5-4)$ and $^{12}\text{CO}(4-3)$ transitions are in good agreement. This is because the ratio between the observed $^{12}\text{CO}(4-3)$ and $^{12}\text{CO}(5-4)$ transitions is compatible with the average CO SLED of SMGs, suggesting that our two interacting sources have similar excitation conditions to the classical SMG population. Despite this, further observations of lower- J CO transitions would be needed to explore whether the high luminosity of the $^{12}\text{CO}(5-4)$ and $^{12}\text{CO}(4-3)$ transitions is due to the presence of a very massive molecular gas reservoir or is affected by a excited gas component. Furthermore, higher-spatial resolution CO observations would be needed to study the CO SLED of each interacting component of SGP 38326 more accurately.

3.2. Dust Continuum Morphology

Although SGP 38326 is resolved into two interacting galaxies, each of them is an extremely luminous starburst in its own right. The dust continuum emission of SMG1 and

Table 1
Properties of SGP 38326 Compared to Other IR-bright Starbursts in the Distant Universe

Source	Redshift	$S_{870\ \mu\text{m}}$ [mJy]	SFR [$M_{\odot}\ \text{yr}^{-1}$]	M_{H_2} [M_{\odot}] ^a	Σ_{SFR} [$M_{\odot}\ \text{yr}^{-1}\ \text{kpc}^{-2}$]	Lensed? ^b	Reference
SGP 38326	4.425	32.5 ± 4.1	$\sim 4500^{\text{c}}$	$\sim 2.7 \times 10^{11}$	$\sim 840/\sim 570^{\text{d}}$	No	This work
GN20	4.055	20.3 ± 2.1	~ 3000	$\sim 1.3 \times 10^{11}$	~ 310	No	Hodge et al. (2012)
HDF 850.1	5.183	7.0 ± 0.4	~ 850	$\sim 3.5 \times 10^{10}$	~ 50	Weakly	Walter et al. (2012)
AzTEC-1	4.342	$17.8 \pm 1.4^{\text{e}}$	~ 2690	$\sim 1.4 \times 10^{11}$	Yun et al. (2015)
AzTEC-3	5.299	$6.20 \pm 0.25^{\text{e}}$	~ 1980	$\sim 5.3 \times 10^{10}$	~ 840	No	Riechers et al. (2014)
HFLS3	6.337	14.3 ± 1.1	~ 2100	$\sim 3.6 \times 10^{10}$	~ 600	Weakly	Riechers et al. (2013)

Notes.

^a Molecular gas masses reported assume an $\alpha_{\text{CO}} = M_{\text{gas}}/L'_{\text{CO}} = 0.8\ \text{K km s}^{-1}\ \text{pc}^2$, typical for high-redshift starbursts and local ULIRGs (Downes & Solomon 1998).

Values taken from the literature have been scaled accordingly.

^b For lensed galaxies, de-magnified values are listed.

^c Total SFR in SGP 38326: $\text{SFR} = \text{SFR}_{\text{SMG1}} + \text{SFR}_{\text{SMG2}}$.

^d Values for SMG1 and SMG2 are given.

^e Measured at 1 mm.

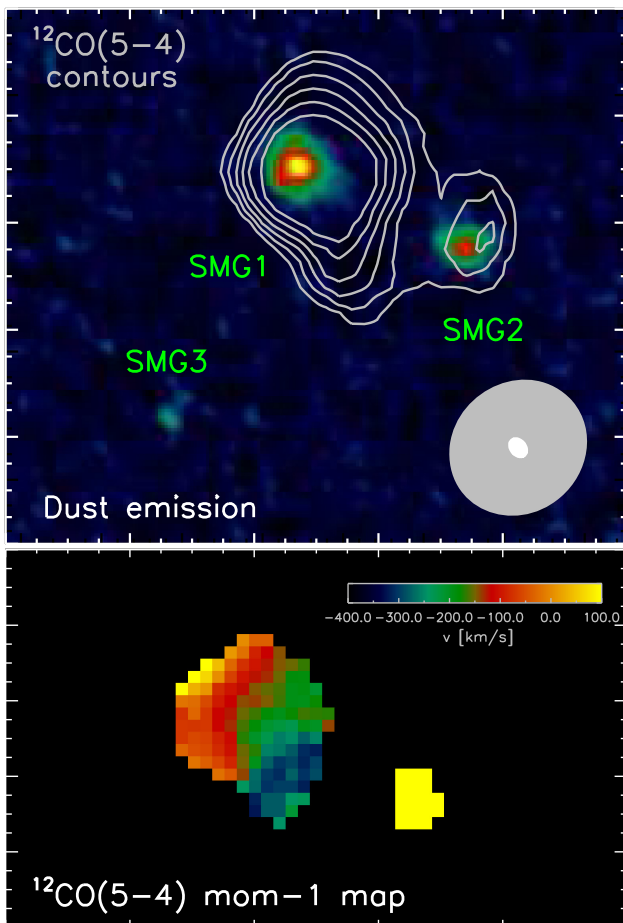


Figure 2. Upper: ALMA $870\ \mu\text{m}$ continuum map of SGP 38326. The three detected SMGs are indicated. The gray contours represent the integrated $^{12}\text{CO}(5-4)$ emission. This line is clearly detected in both SMG1 and SMG2, but there is no $^{12}\text{CO}(5-4)$ detection in SMG3. The beam sizes of the $^{12}\text{CO}(5-4)$ (gray ellipse, $1''.1 \times 1''.0$) and dust continuum (white ellipse, $0''.16 \times 0''.12$) observations are shown, and clearly highlight the impressive increase in spatial resolution. Bottom: velocity map of SMG1 derived from the $^{12}\text{CO}(5-4)$ emission using moment masking (Dame 2011). It can be seen that, despite the lack of spatial resolution, the $^{12}\text{CO}(5-4)$ observations already indicate that SMG1 presents a disk-like rotation. In both panels, north is up and east is left.

SMG2 (rest-frame $160\ \mu\text{m}$) is relatively smooth (see contours in Figure 3). At this spatial resolution, there is no clear evidence of clumpy emission in SMG1 and SMG2. The

physical extent of the dust emission has been measured from a two-dimensional elliptical Gaussian profile fit. Table 2 shows the FWHM of the major and minor axis of each of the components of SGP 38326. These values are similar to the average size of the classical SMG population (Simpson et al. 2015a) and compatible with the size of $z > 3$ SMGs in Ikarashi et al. (2015). SMG1 and SMG2 are, however, considerably smaller than the dust emission in GN20: $\sim 5.3\ \text{kpc} \times 2.3\ \text{kpc}$ (Hodge et al. 2015).

Their size, in combination with their IR-derived SFR (see Table 2), imply that SMG1 and SMG2 have median SFR surface densities of $\Sigma_{\text{SFR}} \sim 840\ M_{\odot}\ \text{yr}^{-1}\ \text{kpc}^{-2}$ and $\Sigma_{\text{SFR}} \sim 570\ M_{\odot}\ \text{yr}^{-1}\ \text{kpc}^{-2}$, respectively. The Σ_{SFR} of SMG1 is very close to the theoretically predicted Eddington limit for starburst disks that are supported by radiation pressure (Andrews & Thompson 2011; Simpson et al. 2015b). Such high Σ_{SFR} values have been only found in a few classical SMGs (Simpson et al. 2015a), in the $z = 6.42$ quasar host galaxy J1148+5251 (Walter et al. 2009) and the dusty starbursts HFLS3 at $z = 6.34$ (Riechers et al. 2013) and AzTEC-3 at $z \sim 5.3$ (Riechers et al. 2014) and are considerably higher than the Σ_{SFR} found in other starbursts at similar redshifts (see Table 1).

Combining the sizes of the dust emission with the molecular gas mass estimates (assuming the molecular gas and dust are roughly co-spatial), we find that the estimated gas surface densities of SMG1 and SMG2 are among the highest ever found (see Table 2). The values found for the SFR surface density, in combination with the derived gas mass surfaces densities, place SMG1 and SMG2 between the sequence of starbursts and “normal” star-forming galaxies in the $\Sigma_{\text{SFR}}-\Sigma_{\text{H}_2}$ plane, with gas depletion timescales between 10 and 100 Myr (Hodge et al. 2015). However, it should be noted that this result assumes that the average CO line ratios for SMGs are valid for SGP 38326.

3.3. Dust Properties and SED Fitting

The SPIRE fluxes for SMG1 and SMG2 are blended within the large SPIRE beam and the signal-noise ratio in the image is not high enough to attempt to deblend them using the ALMA $870\ \mu\text{m}$ positions. Instead we fit the global SED of both sources using both optically thin and optically thick modified black bodies to derive the dust temperatures and dust masses, as well as the integrated IR luminosity. To get the values for each

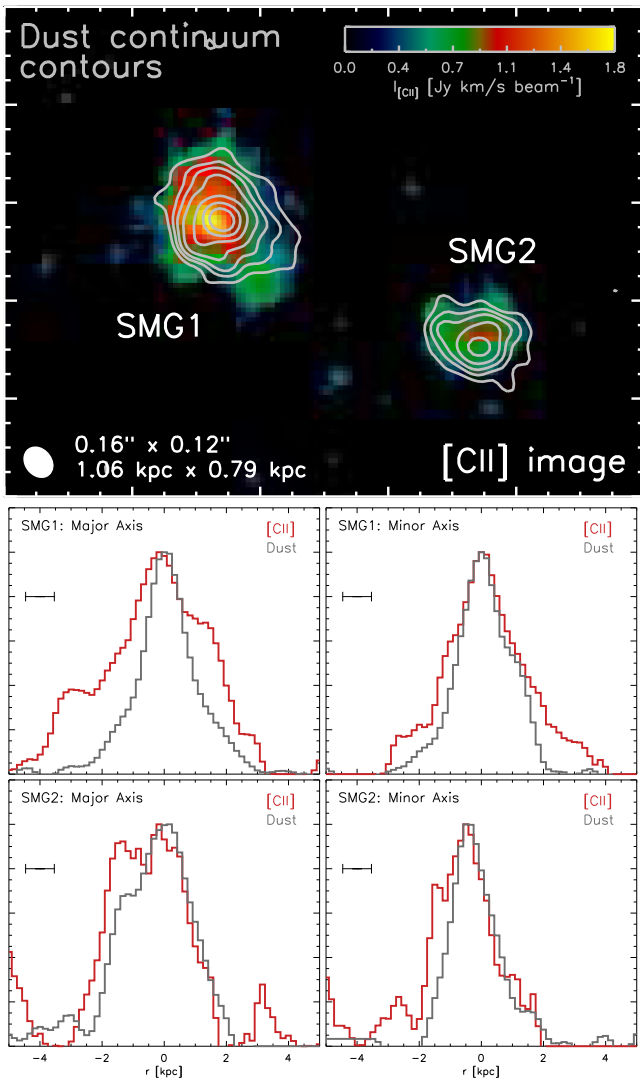


Figure 3. Morphology and spatial extent of the gas and dust in our two distant interacting starbursts. In the top panel, the background image is the integrated [C II] emission created by using moment masking (Dame 2011), while gray contours represent dust emission at rest-frame $160 \mu\text{m}$. Contours are plotted from 3σ to 7σ in steps of 2σ and from 10σ to 25σ in steps of 5σ , where $\sigma = 0.11 \text{ mJy beam}^{-1}$. The two interacting galaxies are separated by a physical distance of $\sim 10 \text{ kpc}$. The beam size is also included. It can be seen that the dust continuum is smooth at the resolution of these data. However, the gas reservoir (as traced by [C II] emission) has an irregular morphology and is extended over larger physical scales. In this panel, north is up and east is left. The bottom panels show the radial profiles (normalized units) of dust and gas along the [C II] major and minor axes of each starburst. The bars represent the spatial resolution of the ALMA high-resolution data. It can be seen that the profiles are significantly different, with [C II] emission being more extended than dust, especially in SMG1.

source separately we have assumed they have the same SED shape and split the IR luminosity and dust mass in the ratio of the $870 \mu\text{m}$ fluxes. Table 2 lists the dust and SED properties. Because of the relatively low SNR of the SPIRE $250 \mu\text{m}$ measurement and only upper limits for PACS, we have no strong preference for either an optically thin or optically thick model; both produce acceptable fits with comparable L_{IR} . What differs strongly between the two models is the dust temperature and accordingly the dust mass which, for a rest frame continuum measurement of $160 \mu\text{m}$, is strongly sensitive to the assumed dust temperature. The optically thin model gives a best fit temperature of $33 \pm 2 \text{ K}$, and dust masses of

Table 2
Observed Properties of Our Two Interacting Dusty Starbursts

	SMG1	SMG2
z_{spec}	4.4237 ± 0.0004	4.4289 ± 0.0004
$S_{870 \mu\text{m}}^{\text{a}}$	$16.3 \pm 1.1 \text{ mJy}$	$7.3 \pm 0.5 \text{ mJy}$
$I_{[\text{C II}]} [\text{Jy km s}^{-1}]$	13.9 ± 1.1	5.3 ± 0.6
$\text{FWHM}_{[\text{C II}]} [\text{km s}^{-1}]$	626 ± 60	585 ± 95
$L_{\text{IR}} [L_{\odot}]$	$(1.6 \pm 0.3) \times 10^{13}$	$(7.9 \pm 0.3) \times 10^{12}$
$\text{SFR} [M_{\odot} \text{ yr}^{-1}]$	~ 2900	~ 1400
$A_{\text{dust}} [\text{kpc}^2]^{\text{b}}$	$2.2 \pm 0.2 \times 2.0 \pm 0.2$	$2.1 \pm 0.2 \times 1.5 \pm 0.1$
$A_{[\text{C II}]} [\text{kpc}^2]^{\text{b}}$	$3.8 \pm 0.1 \times 2.9 \pm 0.1$	$2.7 \pm 0.1 \times 2.1 \pm 0.1$
$\Sigma_{\text{SFR}} [M_{\odot} \text{ yr}^{-1} \text{ kpc}^{-2}]$	~ 840	~ 570
$M_{\text{H}_2} [M_{\odot}]$	$\sim 1.9 \times 10^{11}$	$\sim 7.6 \times 10^{10}$
$M_{\text{dust}}^{\text{c}} [M_{\odot}]$	$\sim 1.9 \times 10^9$	$\sim 6.9 \times 10^8$
$\Sigma_{\text{H}_2} [M_{\odot} \text{ pc}^{-2}]$	$\sim 5.6 \times 10^4$	$\sim 3.1 \times 10^4$
$T_{\text{dust}}^{\text{c}} [\text{K}]$	~ 33	~ 34
$L_{[\text{C II}]} [L_{\odot}]$	$(8.3 \pm 0.2) \times 10^9$	$(2.9 \pm 0.2) \times 10^9$

Notes.

^a Flux densities derived from the ALMA $870 \mu\text{m}$ observations (Section 2) after primary beam attenuation correction. At the high signal to noise of the $870 \mu\text{m}$ detections, the effect of flux boosting is negligible (Oteo et al. 2016).

^b The reported values of the size of dust and [C II] emission are $\text{FWHM}_{\text{major}} \times \text{FWHM}_{\text{minor}}$, where $\text{FWHM}_{\text{major}}$ and $\text{FWHM}_{\text{minor}}$ are obtained from a two-dimensional elliptical Gaussian profile fit to the observed emission.

^c Values obtained assuming optically thin models.

$M_{\text{d}}(\text{SMG1}) = 1.9 \times 10^9 M_{\odot}$ and $M_{\text{d}}(\text{SMG2}) = 6.9 \times 10^8 M_{\odot}$, using a value of $\beta = 2$ and $\kappa_{850} = 0.077 \text{ m}^2/\text{kg}^{-1}$ (Dunne & Eales 2001). This dust temperature would be remarkably low for such a highly star forming galaxy in the local universe but it is now well established that high- z SMGs have much cooler SEDs for their infrared luminosity than do local ULIRGs, due to the more widespread nature of their star formation (Chapman et al. 2004; Hwang et al. 2010; Elbaz et al. 2011; Symeonidis et al. 2013). The optically thick fit gives a higher dust temperature of 55 K , with a correspondingly lower dust mass of $5.6 \times 10^8 M_{\odot}$ and $2.1 \times 10^8 M_{\odot}$ for SMG1 and SMG2, respectively. The optical depth at $100 \mu\text{m}$ is $\tau_{100} \sim 3$ in both galaxies. Dust is a good tracer of molecular gas at both high and low redshift and is increasingly being used as an alternative to, or consistency check for CO derived measurements (Rowlands et al. 2014; Berta et al. 2015; Scoville et al. 2016). The derived gas mass and optically thin dust masses imply gas to dust ratios of $M_{\text{g}}/M_{\text{d}} \sim 101$ and ~ 110 for SMG1 and SMG2, respectively. These values are compatible with those found for starbursts at similar redshifts (Magdis et al. 2011), $z \sim 0.5$ – 1.5 main-sequence galaxies and classical SMGs (Magdis et al. 2012), local star forming spirals (Leroy et al. 2011; Sandstrom et al. 2013) and local LIRGs and ULIRGs (Solomon et al. 1997; Dunne & Eales 2001).

If we instead use the more likely optically thick mass estimates we find higher gas-to-dust ratios by a factor of ~ 3 , but in the extreme conditions of these starbursts it would not be surprising to find both optically thick dust SEDs and highly excited molecular gas, both of which would lower the estimated molecular gas content by a factor of a few.

3.4. Morphology of [C II] Emission

The [C II] spectrum of the two merging components of SGP 38326 is shown in Figure 1. SMG1 has a broad [C II] line ($626 \pm 60 \text{ km s}^{-1}$ FWHM, $L_{[\text{C II}]} / L_{\odot} = (8.3 \pm 0.2) \times 10^9$),

considerably broader than the [C II] emission in other SMGs at similar redshifts (Swinbank et al. 2012; Walter et al. 2012; De Breuck et al. 2014; Riechers et al. 2014) and also broader than local ULIRGs (Farrah et al. 2013). The [C II] emission from SMG2 is slightly narrower ($585 \pm 95 \text{ km s}^{-1}$ FWHM, $L_{[\text{C II}]} = (2.9 \pm 0.2) \times 10^9 L_{\odot}$), with its center shifted $\sim 300 \text{ km s}^{-1}$ with respect to SMG1. The [C II] emission in SMG1 and SMG2 implies that their redshifts are $z_{\text{SMG1}} = 4.4237 \pm 0.0004$ and $z_{\text{SMG2}} = 4.4289 \pm 0.0004$, respectively. The escape velocity of the system (assuming a mass at least as high as the molecular gas mass) is significantly greater than the velocity offset between SMG1 and SMG2, meaning that the galaxies are likely destined to merge, in contrast to multiple HyLIRGs seen at lower redshifts (Iverson et al. 2013). Therefore, our results support a scenario where at least a subset of the most distant starbursts formed in the same highly dissipative mergers of gas-rich galaxies that seem ubiquitous among SMGs at $z < 3$ and local ULIRGs (Engel et al. 2010). This result is in agreement with Narayanan et al. (2015), which claimed that major mergers are common at $z > 4$ and indeed drive some short-lived burst in star formation.

The smooth dust morphology contrasts with the more irregular [C II] emission (Figure 3). [C II] can be associated with many ISM phases, such as photodissociation regions associated with star formation (Stacey et al. 1999), the diffuse or dense molecular medium (Wolfire et al. 2010) and atomic and ionized gas (Madden et al. 1997). Additionally, [C II] can be enhanced by shocks (Appleton et al. 2013) and altered by outflows (Cicone et al. 2015). In the [C II] velocity maps shown in Figure 4 there is no evidence for atomic outflows. Therefore, shock enhancement, local star formation conditions, and tidal forces triggered by the interaction between the components, coupled with local excitation differences are the most likely explanations of the different morphologies of [C II] and dust.

Figure 3 also shows the profiles of the [C II] and dust emission along the major and minor axis of the [C II] emission of each starburst. In addition to their different morphology, the gas traced by [C II] is extended over larger physical scales than the dust (Tacconi et al. 2006; Iverson et al. 2011) and also has significantly different radial profiles. This is further supported by the same 2D Gaussian fitting used to determine the size of the dust emission. The size of the [C II] emission is $3.8 \pm 0.1 \text{ kpc} \times 2.9 \pm 0.1 \text{ kpc}$ in SMG1 and $2.7 \pm 0.1 \text{ kpc} \times 2.1 \pm 0.1 \text{ kpc}$ in SMG2 (FWHM values are quoted here). Therefore, we find that [C II] is extended over a spatial scale larger than that found for dust (Section 3.2). This is in agreement with what has been reported in other $z > 4$ sources, such as ALESS 73.1 (De Breuck et al. 2014), AzTEC-3 (Riechers et al. 2014), HFLS3 (Riechers et al. 2013), and W2246-0526 (Díaz-Santos et al. 2016), but at lower spatial resolution compared with the extension of the emission.

3.5. OH 163 μm Emission

The default continuum observations also covered the 163 μm OH(${}^2\Pi_{1/2}J = 3/2 \rightarrow 1/2$) doublet (whose components are at $\nu_{\text{rest}} = 1834.74735$ and 1834.74735 GHz). We note that the nearby ${}^{12}\text{CO}(16-15)$ emission line is out of the spectral range covered. We present in Figure 1 the OH spectrum of SMG1 extracted in the area where dust emission is detected. We also show the OH spectrum of SMG1 extracted on the position where the dust emission peaks and using an aperture the size of

the synthesized beam. Assuming the redshift determined by the CO lines, the two components of the OH doublet should be located at the velocities marked by the short vertical gray lines. Despite the clear detection of the continuum, no OH emission is detected at the expected velocities. However, there is an emission line in the blue spectrum shifted by $\sim 200 \text{ km s}^{-1}$ blueward that might be associated with the OH doublet since there is no other emission line that could lie at that frequency. An absorption line is apparent in the spectrum of SMG1 $\sim 100 \text{ km s}^{-1}$ redward of the expected position of any OH emission. However, the centers of the emission and absorption do not match with the redshifted components of the OH doublet. After continuum subtraction, Riechers et al. (2014) derived for AzTEC-3 a [C II] peak flux of about 18 mJy and a [OH] peak flux of about 2 mJy. This means a ratio of [C II]/OH ~ 10 . The peak [C II] flux in SMG1 is ~ 20 mJy, and assuming the same [C II]/OH ratio as in AzTEC-3, we would expect the OH emission to have a peak line flux of ~ 2 mJy, in agreement with the peak flux of the emission line seen in the bottom panel of Figure 1. If the detected emission line is actually one of the OH components, its width ($\sim 85 \text{ km s}^{-1}$) is lower than that previously found in strong starbursts in the distant universe (Riechers et al. 2013, 2014). We note that these are the only two cases where OH 163 μm emission has been clearly detected in $z > 4$ starbursts. The putative OH emission in SMG1 is also very compact, being spatially coincident with the maximum of the dust continuum emission. It should be pointed out that the OH emission is only seen where the dust emission is maximum. In contrast, the absorption is seen across the whole disk (Figure 1).

3.6. Dynamics at High Resolution from [C II] Emission

The signal-to-noise of the [C II] detection allows us to study the dynamics of SMG1 and SMG2 at a level of detail never previously achieved for any $z > 4$ unlensed starburst. We present in Figure 4 the [C II] emission in all the velocity channels where it is detected. We have identified six different velocity gradients in SMG1 and one in SMG2, which reveal that both components of SGP 38326 are ordered rotating disks, as corroborated by the [C II] velocity and velocity dispersion maps shown in Figure 5. It should be noted that the velocity field derived in SMG1 from [C II] is very similar to that obtained from the ${}^{12}\text{CO}(5-4)$ transition (see Figure 2), but with about $10\times$ times better spatial resolution. We have fitted the observed velocity field using a disk plus dark matter halo model. We should also note that, since the rotation curve does not turn over, the disk+halo model is degenerate. In any case, if it is a settled disk, it must be massive, with $v_c \sim 300 \text{ km s}^{-1}$ and with a best-fit inclination of ~ 65 deg. This suggests a dynamical mass $M_{\text{dyn,SMG1}} \sim 5 \times 10^{10} M_{\odot}$. The dynamical analysis from [C II] emission at high-spatial resolution indicates that the wide, unresolved CO emissions in SGP 38326 (see Figure 1) are driven by the interaction of two disks separated by $\sim 200 \text{ km s}^{-1}$ in velocity space. This is the opposite of, for example, AzTEC-3, where the [C II] emission (which has half the width of the [C II] emission in SMG1) is supported by emission from a highly dispersed gas (Riechers et al. 2014).

It should be pointed out that the derived dynamical mass is $\sim 5\times$ lower than the molecular gas mass estimated either from CO or the optically thin dust SED fit. However, there are considerable uncertainties involved in the calculation of both of these quantities. The dynamical mass estimate is uncertain by at

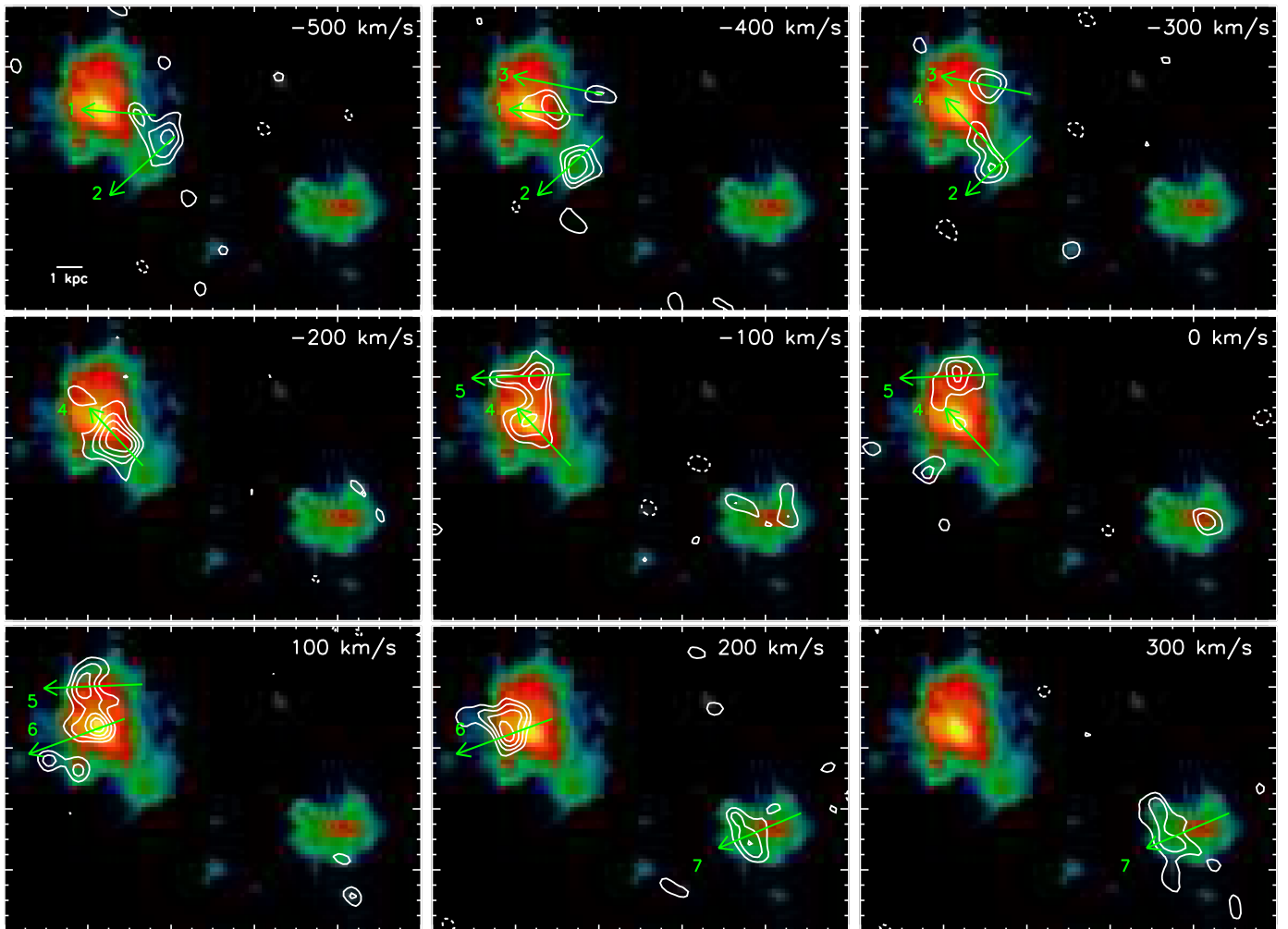


Figure 4. Dynamics of SGP 38326 at high-spatial resolution from [C II] emission: [C II] velocity channel contours are overlaid on the [C II] moment-0 map. The velocity channels have been averaged over 100 km s^{-1} . Contours in the velocity channels start at $\pm 3\sigma$ and are represented in steps of 1σ ($1\sigma = 0.66 \text{ mJy beam}^{-1}$). Green arrows and associated numbers indicate the velocity gradients identified in the continuum-subtracted [C II] data cube.

least by a factor of ~ 2 due to the uncertainty in the inclination of the disk and the merger state. The estimation of the molecular gas mass assumes an α_{CO} factor (we used the value typically assumed for ULIRGs, see above) and a ratio between the $^{12}\text{CO}(5-4)$ and $^{12}\text{CO}(1-0)$ transitions. The derived molecular gas mass would be lower than the obtained value if α_{CO} is actually lower or if the mid- J CO lines are more excited than the average SMG.

We have also determined the dynamical mass of SMG1 and SMG2 by using the isotropic virial estimator (Tacconi et al. 2008; Förster Schreiber et al. 2009; Engel et al. 2010):

$$M_{\text{dyn,vir}} = 2.8 \times 10^5 \Delta v_{\text{FWHM}}^2 R_{1/2}, \quad (1)$$

where Δv_{FWHM} is the width of the integrated [C II] line of each component and $R_{1/2}$ is the radius of the size of the [C II] emission. Since the size of the [C II] emission in SMG1 and SMG2 was derived by assuming elliptical Gaussian profiles (see Section 3.4), $R_{1/2}$ is assumed to be the average value of the semimajor and minor axis (measured from FWHM). The derived dynamical masses with this method for SMG1 and SMG2 ($M_{\text{dyn}}^{\text{SMG1}} \sim 3.6 \times 10^{11} M_{\odot}$ and $M_{\text{dyn}}^{\text{SMG2}} \sim 2.3 \times 10^{11} M_{\odot}$) are now higher than the molecular gas masses. As pointed out in

Engel et al. (2010), the scaling factor appropriate for a rotating disk at an average inclination is a factor of ~ 1.5 smaller (Bothwell et al. 2010). Applying this correction to our measurements, the derived dynamical masses would still be higher than the molecular gas masses. In any case, to carry out a meaningful comparison between the molecular gas and dynamical mass and put constraints on the α_{CO} conversion factor, low- J CO observations would be needed.

We now examine whether the two disks in SGP 38326 are stable by using the Toomre parameter Q (Toomre 1964), which characterizes the stability of a disk against gravitational fragmentation. In this sense, a disk is stable if $Q > 1$. We calculate the Toomre parameter by following Swinbank et al. (2015): $Q = \sigma_r \kappa / \pi G \Sigma_{\text{gas}}$, where $\kappa = a v_{\text{max}} / R$ is the epicyclic frequency (with $a = \sqrt{3}$), σ_r is the radial velocity dispersion, and Σ_{H_2} is the gas mass surface density. All the dynamical parameters are obtained from the [C II] emission. We obtain $Q^{\text{SMG1}} \sim 0.22$ and $Q^{\text{SMG2}} \sim 0.35$, indicating that the two disks are unstable. For comparison, Swinbank et al. (2015) obtained $Q = 0.30 \pm 0.10$ for SDP.81, a strongly lensed galaxy at $z \sim 3$ observed with ALMA at very high spatial resolution (ALMA Partnership et al. 2015; Dye et al. 2015), while De Breuck et al. (2014) obtained an average $Q = 0.58 \pm 0.15$ for a $z \sim 4.8$

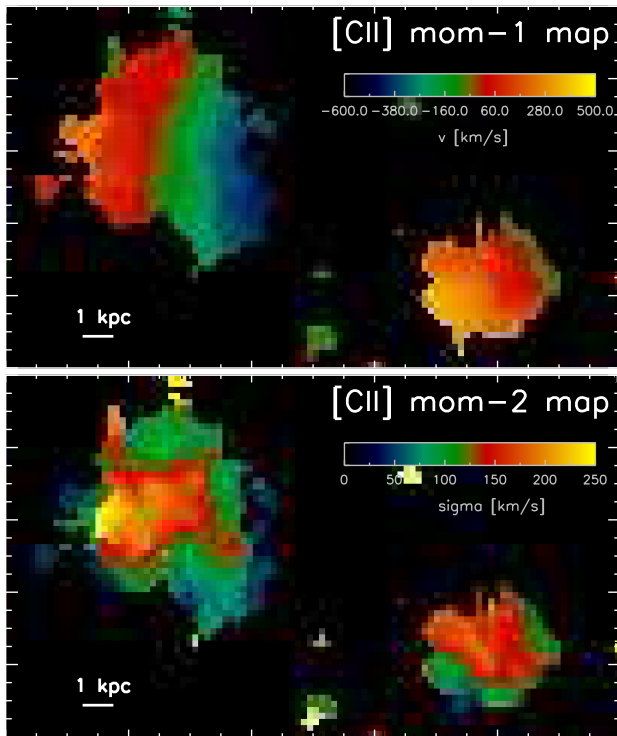


Figure 5. Resolved velocity (upper) and velocity dispersion (bottom) maps of the two interacting components in SGP 38326 obtained from their [C II] emission by using moment masking (Dame 2011). As Figure 4 suggests, all velocity gradients found in SMG1 and SMG2 are compatible with ordered rotation, although with some perturbations, likely due to the effect of the ongoing merger.

starburst containing an AGN. It should be noted that the derived value of the Toomre parameters relies on the validity for SGP 38326 of the average CO line ratio for SMGs. This uncertainty is also present in previous works (De Breuck et al. 2014; Swinbank et al. 2015).

3.7. The Spatially Resolved $L_{[\text{C II}]} / L_{\text{IR}}$ Ratio

Our high-spatial resolution observations also allow us to obtain the first resolved $L_{[\text{C II}]} / L_{\text{IR}}$ ratio map in a dusty starburst at $z > 4$. We have obtained the $L_{[\text{C II}]} / L_{\text{IR}}$ ratio map by simply dividing the $L_{[\text{C II}]}$ and L_{IR} maps. It should be noted that no convolution is required since the spatial resolution of the [C II] and dust continuum map is the same. The $L_{[\text{C II}]}$ map has been obtained from the [C II] moment-0 map by converting the line intensities in each pixel into line luminosities. The L_{IR} map has been derived from the observed $870 \mu\text{m}$ dust continuum map by using the best-fit template to the *Herschel* and SCUBA2 photometry of SGP 38326.

The distinct dust and [C II] morphology leads to a complex spatial distribution for the [C II] to L_{IR} ratio (Figure 6), which is higher in the outer parts of the two starbursts and lower in their centers. This is in agreement with what is observed for local LIRGs (Díaz-Santos et al. 2014). It should be noted that the yellow regions in Figure 6 indicate a lower limit for the $L_{[\text{C II}]} / L_{\text{IR}}$ ratio since they correspond to regions where dust continuum has not been detected, but where there is detectable [C II] emission (recall that [C II] is extended over a larger area than the dust; Section 3.4). Explaining the irregular morphology of the $L_{[\text{C II}]} / L_{\text{IR}}$ ratio is challenging due to the many

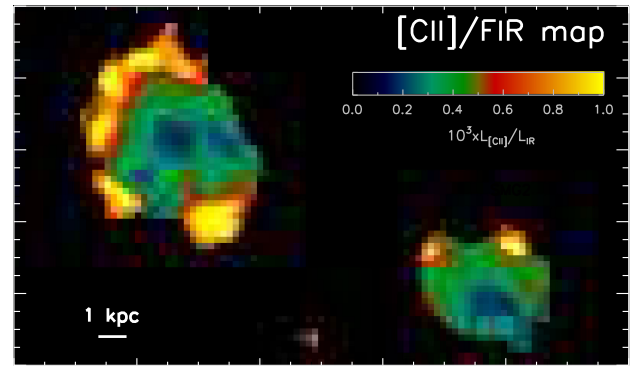


Figure 6. Resolved $L_{[\text{C II}]} / L_{\text{IR}}$ ratio map for our pair of SMGs. The L_{IR} for each pixel has been calculated from the observed flux density and using an extrapolation based on the median SED of SMGs in the ALESS survey (Swinbank et al. 2014), which produces a good fit to our photometric data points. The different morphology of dust and [C II] means that the [C II]/FIR ratio is higher in the outer parts of the galaxies and lower in the center (where the peak of dust continuum emission is located). It should be noted that the yellow regions actually represent a lower limit of the $L_{[\text{C II}]} / L_{\text{IR}}$ ratio, since they correspond to regions where dust emission is not detected at $>3\sigma$.

phases of the ISM giving rise to [C II] emission (see Section 3.4). The most likely explanations are different excitation conditions for [C II] and variable dust optical depth across the disks. The presence of an AGN can also lower the $L_{[\text{C II}]} / L_{\text{IR}}$ ratio (Díaz-Santos et al. 2013), so an AGN could therefore be responsible for the low values of the $L_{[\text{C II}]} / L_{\text{IR}}$ ratio in the center of the galaxies and in their integrated values (see below). While we have no direct evidence for an AGN with the present data, the existence of one would not be surprising since AGNs seem to be ubiquitous in the strongest starbursts at lower redshifts (Ivison et al. 2013).

Larger samples of galaxies would be needed to explore at high resolution whether these gradients are present in most of the population of dusty starbursts at $z > 4$ and also in less extreme star forming systems.

Figure 7 compares the integrated values of the $L_{[\text{C II}]} / L_{\text{IR}}$ ratio with sources at similar redshifts and in the local universe. The left panel of Figure 7 shows that the values found for the $L_{[\text{C II}]} / L_{\text{IR}}$ ratio in SMG1 and SMG2 are similar to those found in other comparably luminous IR galaxies at similar and higher redshifts (Swinbank et al. 2012; Walter et al. 2012; De Breuck et al. 2014; Riechers et al. 2014; Díaz-Santos et al. 2016) and in the local universe (Díaz-Santos et al. 2013). Our two interacting starbursts are at the upper end of the L_{IR} distribution of $z > 4$ galaxies, suggesting that the anti-correlation between $L_{[\text{C II}]} / L_{\text{IR}}$ ratio and L_{IR} seen in the local universe holds up to $z \sim 4$, but with an offset in L_{IR} .

We also present in Figure 7 the individual pixel values of the $L_{[\text{C II}]} / L_{\text{IR}}$ ratio for SMG1 and SMG2. Since the synthesized beam is sampled by approximately 5 pixels on each side, we have re-binned the $L_{[\text{C II}]} / L_{\text{IR}}$ ratio map every 5 pixels, so each new pixel approximately samples the area of one synthesized beam. Average values across contiguous pixels are taken during map re-sizing. For those regions with [C II] but no dust continuum detection, we have given lower limits instead. The individual pixel values suggest that galaxy regions associated with higher star formation (or higher dust surface density) have lower $L_{[\text{C II}]} / L_{\text{IR}}$ ratios.

A tight correlation between the $L_{[\text{C II}]} / L_{\text{IR}}$ ratio and the IR surface density has been reported in local galaxies (Lutz

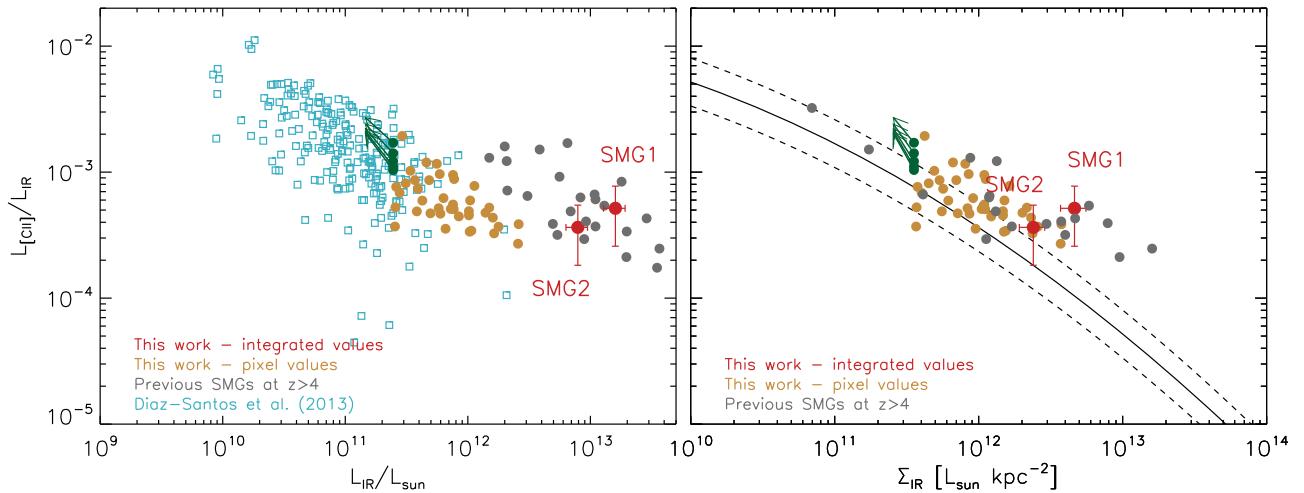


Figure 7. $[\text{C II}]$ to L_{IR} ratio for our pair of interacting starbursts as a function of their total IR luminosity (left) and their IR surface density (right). On the left panel, the values for the two SMGs in SGP 38326 are shown and compared with previous results for submillimeter galaxies at similar or higher redshifts (Swinbank et al. 2012; Walter et al. 2012; Riechers et al. 2013, 2014; De Breuck et al. 2014; Rawle et al. 2014; Gullberg et al. 2015; Díaz-Santos et al. 2016; Spilker et al. 2016) and with local IR-bright galaxies (Díaz-Santos et al. 2013). On the right panel, the black curve represents the best-fit for local galaxies in Lutz et al. (2016), with the dashed curves representing the scatter of the local relation. In both panels, we represent the individual pixel values for SMG1 and SMG2 after resampling the pixels to make them match with the size of the synthesized beam (see the text for details). Green dots with arrows indicate upper limits of the $L_{[\text{C II}]} / L_{\text{IR}}$ and correspond to regions where there is $[\text{C II}]$ emission but no dust continuum detection at 3σ . The IR luminosities in Díaz-Santos et al. (2013) have been converted to $L_{8-1000 \mu\text{m}}$ by multiplying by a 1.8 factor. For lensed sources, the values included have been corrected for gravitational amplification. Our SMGs are on the bright side of the brightness distribution of previous SMGs with $[\text{C II}]$ detections, and they also have among the lowest $L_{[\text{C II}]} / L_{\text{IR}}$ ratios. Moreover, there is an indication that galaxies with the highest SFR and star formation surface density (SMG1, AzTEC-3, and HFLS3) tend to depart from the local relation toward higher values of the $L_{[\text{C II}]} / L_{\text{IR}}$ ratio.

et al. 2016). This relation and its typical scatter is represented in the right panel of Figure 7 along with the derived values for SMG1 and SMG2 (both integrated values and individual pixel values) and other $z > 4$ starbursts with measured sizes. We have defined the IR surface density as $\Sigma_{\text{IR}} = L_{\text{IR}} / (\pi R_a R_b)$, where R_a and R_b are the major and minor axis radii (derived by FWHM/2 from a elliptical Gaussian profile) of the continuum dust emission of each galaxy.

We see in Figure 7 that SMG1 and SMG2 (and also most individual pixel values) tend to depart from the local relation, having slightly higher $L_{[\text{C II}]} / L_{\text{IR}}$ values for a given IR surface density. The same happens with the most extreme sources at high redshift such as AzTEC-3 or HFLS3. SMG1, AzTEC-3, and HFLS3 are close to the Eddington limit. This might indicate that the $[\text{C II}]$ emission in those galaxies might be excited by an outflow or shocks from a possible AGN. In fact, strong OH $163 \mu\text{m}$ emission has been detected in AzTEC-3 and HFLS3 (Riechers et al. 2013, 2014), supporting the presence of outflowing material. However, no clear signature of OH $163 \mu\text{m}$ emission or outflowing material (apart from the extended $^{12}\text{CO}(5-4)$ emission shown in Figure 2) has been detected in SMG1 (see Section 3.5), leaving unknown the reason of its enhanced $L_{[\text{C II}]} / L_{\text{IR}}$ ratio with respect to its IR surface density.

4. CONCLUSIONS

In this work we have presented ALMA high-spatial resolution ($\sim 0''.1$ or ~ 800 pc) imaging of the gas and dust in SGP 38326, an interacting pair of luminous IR starbursts at $z = 4.425$. Despite the redshift of the two galaxies being unknown when the ALMA $870 \mu\text{m}$ continuum observations were defined, the $[\text{C II}]$ and OH emission lines were serendipitously covered by the continuum spectral setup. This offered the opportunity of studying at high resolution the properties of the ISM in the likely progenitor of a massive,

elliptical galaxy at $z \sim 3$. The main conclusions of our work are:

1. The dust continuum emission (rest-frame $160 \mu\text{m}$) in our pair of interacting starbursts at $z = 4.425$ presents a relatively smooth distribution at the resolution of our data and is distributed over an area of $2.2 \pm 0.2 \text{ kpc} \times 2.0 \pm 0.2 \text{ kpc}$ in SMG1 and $2.1 \pm 0.2 \text{ kpc} \times 1.5 \pm 0.1 \text{ kpc}$ in SMG2 (values quote FWHM of a 2D Gaussian elliptical profile), similar to that seen in the bulk of SMGs at $z = 2-3$. However, the gas traced by $[\text{C II}]$ emission has a more irregular morphology and is more extended than the gas, being extended over an area of $3.8 \pm 0.1 \text{ kpc} \times 2.9 \pm 0.1 \text{ kpc}$ in SMG1 and $2.7 \pm 0.1 \text{ kpc} \times 2.1 \pm 0.1 \text{ kpc}$ in SMG2.
2. A dynamical analysis of the resolved $[\text{C II}]$ emission revealed that the velocity fields of the two interacting components of SGP 38326 are compatible with disk-like ordered rotation, in contrast with claims for other extreme IR-bright starburst in the early universe. The velocity field of the two interacting starbursts does not show any clear sign of outflowing material. In fact, the OH $163 \mu\text{m}$ emission line (a tracer of molecular outflows), if present, is much fainter and narrower than in other extreme starbursts in the early universe.
3. Our high-resolution observations allowed us to build the first resolved $L_{[\text{C II}]} / L_{\text{IR}}$ map of a dusty starburst at $z > 4$. Due to the different morphologies of the dust and gas, the $L_{[\text{C II}]} / L_{\text{IR}}$ ratio is lower in the center of the galaxies and higher in the outer parts, where there is $[\text{C II}]$ emission but no continuum is detected at $>3\sigma$. This is consistent with what has been reported in the local universe. The pixel values on the $L_{[\text{C II}]} / L_{\text{IR}}$ map suggest that regions with higher star formation have lower associated $L_{[\text{C II}]} / L_{\text{IR}}$ values.

4. Our results support a scenario where the most distant starbursts were formed in the same highly dissipative mergers of gas-rich galaxies that seem ubiquitous among SMGs at $z < 3$, in agreement with recent simulation of IR-bright sources in the early universe.

Systems like SGP 38326 are truly important for understanding early massive galaxy formation. The SFR of SGP 38326 will decline with an e -folding timescale of $\tau_{\text{gas}} \sim 100$ Myr. This assumes a Salpeter IMF and $\tau_{\text{gas}} = 2 \times M(\text{H}_2)/\text{SFR}$, where the factor of two accounts for the 50% gas recycling in stellar evolution (Fu et al. 2013). This is a simplistic approach since it does not include the possible effect of gas outflow and inflow, but we can assume that they roughly compensate each other during galaxy growth (if there are strong outflows, τ_{gas} would be even lower). With that timescale, all the gas would have been consumed in ~ 0.5 Gyr (or ~ 1 Gyr if Chabrier IMF was assumed). Therefore, our extremely bright interacting starbursts are the likely progenitor of a massive elliptical at $z \sim 3$. Assuming that all molecular gas is converted into stars, the stellar mass of the resulting elliptical galaxy would be $M_* \sim 2.7 \times 10^{11} M_{\odot}$, well in line with the values found for ultra-massive galaxies at $z \sim 3$ (Marsan et al. 2015). We are, consequently, witnessing the formation of the red sequence of galaxies (Kriek et al. 2008).

I.O., R.J.I., Z.Y.Z., L.D., A.L. and S.M. acknowledge support from the European Research Council in the form of the Advanced Investigator Programme, 321302, COSMICISM. L.D. and S.J.M. also acknowledge support from European Research Council Consolidator Grant, Cosmic Dust. I.R.S. acknowledges support from STFC (ST/L00075X/1), the ERC Advanced Investigator programme DUSTYGAL 321334 and a Royal Society/Wolfson Merit Award. H.M. acknowledges support from the Fundação para a Ciência e a Tecnologia (FCT) through the Fellowship SFRH/BPD/97986/2013. This paper makes use of the following ALMA data: ADS/JAO.ALMA#2013.1.00001.S and ADS/JAO.ALMA#2013.1.00449.S. ALMA is a partnership of ESO (representing its member states), NSF (USA) and NINS (Japan), together with NRC (Canada) and NSC and ASIAA (Taiwan) and KASI (Republic of Korea), in cooperation with the Republic of Chile. The Joint ALMA Observatory is operated by ESO, AUI/NRAO and NAOJ. The H-ATLAS is a project with *Herschel*, which is an ESA space observatory with science instruments provided by European-led Principal Investigator consortia and with important participation from NASA. The H-ATLAS website is <http://www.h-atlas.org/>.

REFERENCES

- ALMA Partnership et al. 2015, *ApJL*, 808, L4
 Andrews, B. H., & Thompson, T. A. 2011, *ApJ*, 727, 97
 Appleton, P. N., Guillard, P., Boulanger, F., et al. 2013, *ApJ*, 777, 66
 Appleton, P. N., Lanz, L., Bitsakis, T., et al. 2015, *ApJ*, 812, 118
 Berta, S., Lutz, D., Genzel, R., Foerster-Schreiber, N. M., & Tacconi, L. J. 2015, *A&A*, 587, 73
 Blain, A. W., Smail, I., Ivison, R. J., Kneib, J.-P., & Frayer, D. T. 2002, *PhR*, 369, 111
 Bothwell, M. S., Chapman, S. C., Tacconi, L., et al. 2010, *MNRAS*, 405, 219
 Bussmann, R. S., Perez-Fournon, I., Amber, S., et al. 2013, *ApJ*, 779, 25
 Bussmann, R. S., Riechers, D., Fialkov, A., et al. 2015, *ApJ*, 812, 43
 Carilli, C. L., Riechers, D., Walter, F., et al. 2013, *ApJ*, 763, 120
 Carilli, C. L., & Walter, F. 2013, *ARA&A*, 51, 105
 Casey, C. M., Chen, C.-C., Cowie, L. L., et al. 2013, *MNRAS*, 436, 1919
 Chapman, S. C., Blain, A. W., Smail, I., & Ivison, R. J. 2005, *ApJ*, 622, 772
 Chapman, S. C., Smail, I., Blain, A. W., & Ivison, R. J. 2004, *ApJ*, 614, 671
 Ciccone, C., Maiolino, R., Gallerani, S., et al. 2015, *A&A*, 574, A14
 Cooray, A., Calanog, J., Wardlow, J. L., et al. 2014, *ApJ*, 790, 40
 Dame, T. M. 2011, arXiv:1101.1499
 De Breuck, C., Williams, R. J., Swinbank, M., et al. 2014, *A&A*, 565, A59
 Diaz-Santos, T., Armus, L., Charmandaris, V., et al. 2013, *ApJ*, 774, 68
 Diaz-Santos, T., Armus, L., Charmandaris, V., et al. 2014, *ApJL*, 788, L17
 Diaz-Santos, T., Assef, R. J., Blain, A. W., et al. 2016, *ApJL*, 816, L6
 Downes, D., & Solomon, P. M. 1998, *ApJ*, 507, 615
 Dunne, L., & Eales, S. A. 2001, *MNRAS*, 327, 697
 Dye, S., Furlanetto, C., Swinbank, A. M., et al. 2015, *MNRAS*, 452, 2258
 Eales, S., Dunne, L., Clements, D., et al. 2010, *PASP*, 122, 499
 Edge, A., Sutherland, W., Kuijken, K., et al. 2013, *Msngr*, 154, 32
 Elbaz, D., Dickinson, M., Hwang, H. S., et al. 2011, *A&A*, 533, A119
 Engel, H., Tacconi, L. J., Davies, R. I., et al. 2010, *ApJ*, 724, 233
 Farrah, D., Lehoucq, V., Spoon, H. W. W., et al. 2013, *ApJ*, 776, 38
 Forster Schreiber, N. M., Genzel, R., Bouche, N., et al. 2009, *ApJ*, 706, 1364
 Fu, H., Cooray, A., Feruglio, C., et al. 2013, *Natur*, 498, 338
 Gabor, J. M., & Davé, R. 2012, *MNRAS*, 427, 1816
 Geach, J. E., Chapin, E. L., Coppin, K. E. K., et al. 2013, *MNRAS*, 432, 53
 Gullberg, B., De Breuck, C., Vieira, J. D., et al. 2015, *MNRAS*, 449, 2883
 Hartley, W. G., Almaini, O., Mortlock, A., et al. 2013, *MNRAS*, 431, 3045
 Hodge, J. A., Carilli, C. L., Walter, F., et al. 2012, *ApJ*, 760, 11
 Hodge, J. A., Riechers, D., Decarli, R., et al. 2015, *ApJL*, 798, L18
 Hodge, J. A., Karim, A., Smail, I., et al. 2013, *ApJ*, 768, 91
 Holland, W. S., Bintley, D., Chapin, E. L., et al. 2013, *MNRAS*, 430, 2513
 Hwang, H. S., Elbaz, D., Magdis, G., et al. 2010, *MNRAS*, 409, 75
 Ikarashi, S., Ivison, R. J., Caputi, K. I., et al. 2015, *ApJ*, 810, 133
 Ivison, R. J., Papadopoulos, P. P., Smail, I., et al. 2011, *MNRAS*, 412, 1913
 Ivison, R. J., Swinbank, A. M., Smail, I., et al. 2013, *ApJ*, 772, 137
 Karim, A., Swinbank, A. M., Hodge, J. A., et al. 2013, *MNRAS*, 432, 2
 Kennicutt, R. C., Jr. 1998, *ARA&A*, 36, 189
 Kodama, T., Tanaka, I., Kajisawa, M., et al. 2007, *MNRAS*, 377, 1717
 Kriek, M., van der Wel, A., van Dokkum, P. G., Franx, M., & Illingworth, G. D. 2008, *ApJ*, 682, 896
 Leroy, A. K., Bolatto, A., Gordon, K., et al. 2011, *ApJ*, 737, 12
 Lutz, D., Berta, S., Contursi, A., et al. 2016, *A&A*, 591, 136
 Madden, S. C., Poglitsch, A., Geis, N., Stacey, G. J., & Townes, C. H. 1997, *ApJ*, 483, 200
 Magdis, G. E., Daddi, E., Elbaz, D., et al. 2011, *ApJL*, 740, L15
 Magdis, G. E., Daddi, E., Bethermin, M., et al. 2012, *ApJ*, 760, 6
 Marsan, Z. C., Marchesini, D., Brammer, G. B., et al. 2015, *ApJ*, 801, 133
 Mei, S., Holden, Brad P., Blakeslee, John P., et al. 2009, *ApJ*, 690, 42
 Narayanan, D., Turk, M., Feldmann, R., et al. 2015, *Natur*, 525, 496
 Oke, J. B., & Gunn, J. E. 1983, *ApJ*, 266, 713
 Oliver, S. J., Wang, L., Smith, A. J., et al. 2010, *A&A*, 518, L21
 Oteo, I., Zwaan, M. A., Ivison, R. J., Smail, I., & Biggs, A. D. 2016, *ApJ*, 822, 360
 Rawle, T. D., Egami, E., Bussmann, R. S., et al. 2014, *ApJ*, 783, 59
 Riechers, D. A., Bradford, C. M., Clements, D. L., et al. 2013, *Natur*, 496, 329
 Riechers, D. A., Carilli, C. L., Capak, P. L., et al. 2014, *ApJ*, 796, 84
 Rosati, P., Tozzi, P., Gobat, R., et al. 2009, *A&A*, 508, 583
 Rowlands, K., Gomez, H. L., Dunne, L., et al. 2014, *MNRAS*, 441, 1017
 Sandstrom, K. M., Leroy, A. K., Walter, F., et al. 2013, *ApJ*, 777, 5
 Scoville, N., Sheth, K., Aussel, H., et al. 2016, *ApJ*, 820, 83
 Simpson, J. M., Smail, I., Swinbank, A. M., et al. 2015a, *ApJ*, 799, 81
 Simpson, J. M., Smail, I., Swinbank, A. M., et al. 2015b, *ApJ*, 807, 128
 Siringo, G., Kreysa, E., Kovacs, A., et al. 2009, *A&A*, 497, 945
 Sobral, D., Smail, I., Best, P. N., et al. 2013, *MNRAS*, 428, 1128
 Solomon, P. M., Downes, D., Radford, S. J. E., & Barrett, J. W. 1997, *ApJ*, 478, 144
 Spilker, J., Marrone, D., Aravena, M., et al. 2016, arXiv:1604.05723
 Stacey, G. J., Swain, M. R., Bradford, C. M., et al. 1999, in *ESA Special Publication*, Vol. 427, The universe as Seen by ISO, ed. P. Cox, & M. Kessler (Noordwijk: ESA), 973
 Stanford, S. A., Romer, A. K., Sabirli, K., et al. 2006, *ApJL*, 646, L13
 Strazzullo, V., Rosati, P., Pannella, M., et al. 2010, *A&A*, 524, A17
 Swinbank, A. M., Karim, A., Smail, I., et al. 2012, *MNRAS*, 427, 1066
 Swinbank, A. M., Simpson, J. M., Smail, I., et al. 2014, *MNRAS*, 438, 1267
 Swinbank, A. M., Dye, S., Nightingale, J. W., et al. 2015, *ApJL*, 806, L17
 Symeonidis, M., Vaccari, M., Berta, S., et al. 2013, *MNRAS*, 431, 2317
 Tacconi, L. J., Neri, R., Chapman, S. C., et al. 2006, *ApJ*, 640, 228
 Tacconi, L. J., Genzel, R., Smail, I., et al. 2008, *ApJ*, 680, 246
 Thomas, D., Maraston, C., Bender, R., & Mendes de Oliveira, C. 2005, *ApJ*, 621, 673

- Thomas, D., Maraston, C., Schawinski, K., Sarzi, M., & Silk, J. 2010, [MNRAS](#), **404**, 1775
- Toomre, A. 1964, [ApJ](#), **139**, 1217
- Tozzi, P., Santos, J. S., Jee, M. J., et al. 2015, [ApJ](#), **799**, 93
- Walter, F., Riechers, D., Cox, P., et al. 2009, [Natur](#), **457**, 699
- Walter, F., Decarli, R., Carilli, C., et al. 2012, [Natur](#), **486**, 233
- Weiß, A., Kovacs, A., Coppin, K., et al. 2009, [ApJ](#), **707**, 1201
- Wolfire, M. G., Hollenbach, D., & McKee, C. F. 2010, [ApJ](#), **716**, 1191
- Yun, Min S., Aretxaga, I., Gurwell, M. A., et al. 2015, [MNRAS](#), **454**, 3485
- Zhu, M., Gao, Y., Seaquist, E. R., & Dunne, L. 2007, [AJ](#), **134**, 118
- Zirm, Andrew W., Stanford, S. A., Postman, M., et al. 2008, [ApJ](#), **680**, 224